Journal of Power Sources 506 (2021) 230212

Contents lists available at ScienceDirect

Journal of Power Sources

journal homepage: www.elsevier.com/locate/jpowsour

Enhancement in charge extraction and moisture stability of perovskite solar cell via infiltration of charge transport material in grain boundaries

Danbi Kim [a], Insoo Shin [b,**], Hyun-Seock Yang [a], Pesi Mwitumwa Hangoma [a], Jong Seong Bae [c], Bo Ram Lee [a], Joo Hyun Kim [d], Doo Kyung Moon [e], Sung Heum Park [a,*]

[a] Department of Physics, Pukyong National University, Busan, 48513, Republic of Korea
[b] Phosphor Bank, Pukyong National University, Busan, 48513, Republic of Korea
[c] Division of Analysis and Research, Korea Basic Science Institute (KBSI), Busan, 46742, Republic of Korea
[d] Department of Polymer Engineering, Pukyong National University, Busan, 48513, Republic of Korea
[e] Department of Chemical Engineering, Konkuk University, Seoul, 05029, Republic of Korea

HIGHLIGHTS

- Interpenetration network of HTM and perovskite has been successfully achieved.
- HTM infiltrated into grain-boundaries of perovskite film via simple MS method.
- Hole extraction has improved via deep infiltration of HTM.
- Defects within the grain-boundaries has passivated via deep infiltration of HTM.
- Stability of MS-device has significantly improved compared to conventional device.

GRAPHICAL ABSTRACT

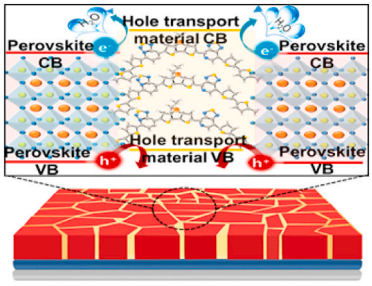

ARTICLE INFO

Keywords:
Inverted perovskite solar cells
Passivation method
Infiltration force
Hole transport materials
Grain growth

ABSTRACT

Perovskite solar cells (PeSCs) attract significant attention owing to their numerous advantages such as superior optical/electrical properties and solution processability. However, the existence of defects in the grain boundaries still prevents high performance and stable PeSCs. Here, we present a simple yet effective momentary spinning (MS) method for passivating defect sites in the grain boundaries of PeSCs. By applying the MS method to the perovskite active layer, we achieve infiltration of p-type hole transporting materials (HTMs) with selective hole transport into grain boundaries, thereby reducing leakage current, suppressing nonradiative recombination loss, and achieving efficient hole extraction. The MS-fabricated PeSCs remarkably enhance device performance, displaying higher short-circuit current (J_{sc}), open-circuit voltage (V_{oc}), and fill factor (FF) than the conventional spin-coating (SC) devices. The best device exhibits a J_{sc} of 23.2 mA cm^{-2}, a V_{oc} of 0.99 V, and an FF of 0.81, yielding a power conversion efficiency (PCE) of 18.6%. In addition, passivating hydrophilic grain boundaries with hydrophobic HTM improves the moisture stability of the device. When device performance is monitored for over 20 days of storage, the MS device exhibits improved stability with over 80% of the initial PCE compared to the SC device with only 50%.

* Corresponding author.
** Corresponding author.
E-mail addresses: factor86@pukyong.ac.kr (I. Shin), spark@pknu.ac.kr (S.H. Park).

https://doi.org/10.1016/j.jpowsour.2021.230212
Received 31 March 2021; Received in revised form 11 June 2021; Accepted 24 June 2021
Available online 2 July 2021

1. Introduction

Inverted (p-i-n) perovskite solar cells (PeSCs) with [6,6]-phenyl--C61-butyric acid methyl ester ($PC_{61}BM$) as the top electron transport layer are strong candidates for promising energy sources owing to their attractive advantages, such as high absorption coefficients, low exciton binding energy, long carrier lifetime, and tunable band gap [1–4]. Accordingly, the device performance of PeSCs has been dramatically improved over several years with the power conversion efficiency (PCE) getting enhanced from 9% to over 23% [5].

Remarkable enhancement in the device performance of PeSC is achieved primarily by obtaining a highly crystalline perovskite active layer with enlarged grains, full coverage, and pinhole-free surface [6–9]. However, enlarged grains inevitably produce apparent grain boundaries, which cause defect sites due to the presence of vacancies, perovskite intermediates, and dangling bonds [10,11]. Increasing grain boundaries increases interfacial carrier recombination, leakage current by the shunting path of grain boundaries, charge accumulation from the energy barrier between the grains, and carrier extraction disturbance with mismatch energy alignment of the interface defect [12–16], and consequently reduces the fill factor (FF) and open circuit voltage (V_{oc}) of the PeSC. Moreover, low device stability is caused owing to the methylammonium (MA^+) cations of conventional $CH_3NH_3PbI_3$ ($MAPbI_3$) perovskite active layers, which are hygroscopic at the grain boundary [17,18].

Several researchers have attempted to reduce grain boundaries by controlling the evaporation speed of the solvent and the direction of grain growth and improving device performance and stability [19–21]. However, the devices exhibit an incomplete perovskite active layer with the appearance of the grain boundaries, and it is difficult to simultaneously obtain reduced grain boundaries with highly crystalline enlarged grains. More recently, a considerable enhancement in the device performance and stability of PeSCs has been demonstrated via passivating grain boundaries using various materials, including 2D perovskite, 3D-2D perovskite adducts [22–25], amine-based small molecules [26], alkylammonium halide [27] or ammonium salts [28], and organic materials [29–32]. Although these studies have well-passivating grain boundaries with enlarged grains, the insulating properties of these materials intrinsically disturb the charge transport and consequently increase the internal resistance of the device [33].

A reasonable approach to passivate grain boundaries is the replacement of the insulating materials with hole transport material (HTM) that have selective carrier transporting properties and optimum energy level [29,34–36]. In particular, infiltration of the HTMs into the perovskite grain boundaries is effective because a soluble HTM enables the passivation of defect sites inside and removes the incomplete perovskite intermediate even at the grain boundaries [37]. Furthermore, the HTM blocks electron injection from the perovskite owing to its upper conduction band edge than that of the perovskite active layer, while it transports the hole to hole transport layer, leading to efficient charge collection at the electrode and suppressed charge accumulation at the grain boundaries.

Despite these advantages, the infiltration of HTM materials has hardly been realized due to the absence of an effective fabrication method with sufficient infiltration force. Insufficient infiltration force into grain boundaries results in random distribution of the HTM materials on the perovskite surface [34,38], and acts as a defect [39]. Therefore, development of an effective fabrication method with sufficient infiltration force is crucial to achieving both efficient charge transport and complete passivation of grain boundaries for high performance and stable PeSC. In this work, we develop an effective momentary spinning (MS) method with controllable infiltration force. By applying momentary spinning in the spin-coating process to form a perovskite active layer, we controlled the infiltration force in the film formation process and achieved infiltration of p-type HTM into the perovskite grain boundaries, which demonstrated a desirable perovskite active layer composed of highly crystalline grains and fully passivated grain boundaries. The device prepared by the MS method exhibits reduced leakage current, suppressed nonradiative recombination loss, and efficient hole extraction with high hole mobility. These properties improved the PCE of PeSC from 16.5% to 18.6% and provided long-term stability.

2. Experimental section

2.1. Materials

Methylammonium iodide (MAI, 99%) was purchased from Alfa Aesar. Lead(II) iodide (PbI_2, 99%) was purchased from Greatcell Solar. Dimethyl sulfoxide (DMSO, 99.9%), N,N-dimethylformamide (DMF, 99.8%), and chlorobenzene (CB) were purchased from Sigma-Aldrich.

2.2. Device fabrication

ITO-coated glass substrates were sequentially cleaned in an ultrasonic bath with deionized water, acetone, ethanol, and isopropanol for 10 min and then dried in an oven at 100 °C overnight. After treatment with UV/Ozone for 1800 s, poly(3,4-ethylenedioxythiophene)-poly (styrene sulfonate) (PEDOT:PSS, Baytron PH) was spin-coated onto the ITO-coated glass substrate at 4500 rpm for 40 s and then annealed at 140 °C for 10 min. For the perovskite layers, a 45 wt % perovskite precursor containing MAI (1.2 M) and PbI_2 (1.1 M) in DMF and DMSO (9:1) was spin-coated at 1200 rpm for 5 s, and CB (300 μL) was quickly dropped on the spinning substrate at 5000 rpm for 50 s. Afterward [6,6],-phenyl-C61-butyric acid methyl ester ($PC_{61}BM$, 30 mg/1 mL) solution in CB was spin-coated onto the perovskite layer at 1200 rpm for 40 s. The as-prepared perovskite film was heated at 120 °C for 10 min in a vacuum oven, and then cooled down to room temperature in the glove box. After that, we carried out CB treatment by using a fully dropped CB solvent onto the perovskite film for uniform film, a PCBM solution spin-coated at 1200 rpm for 40 s. For the Filled-perovskite grain boundary with hole transport materials (MS film), the HTM (p-DTS($fbtth_2$)$_2$, PCDTBT, P3HT, PTB7-Th) with a concentration of 0.5 (% w/v) in CB was first dropped onto the perovskite film, then spin coated 1s at 2000 rpm for permeating the perovskite grain boundary. Then, the CB solvent was deposited during 2000 rpm for washing only top surface of HTM, and a spin-coated PCBM solution at 1200 rpm for 40 s after drying. Finally, aluminum (Al) was deposited as the top cathode (100 nm) at thermal evaporation under 5×10^{-7} Torr. The PeSC device was fabricated with the following structures: ITO/PEDOT:PSS/$MAPbI_3$ (with or without HTM)/$PC_{61}BM$/Al.

2.3. Characterization

The contact angle and surface tension were measured using a UNICAM(GITSOFTTECH) system. The p-DTS($fbtth_2$)$_2$ with different concentration (from 0 %w/v to 1.3% w/v) in CB solution was dropped on the polytetrafluoroethylene(PTFE) substrate to measure contact angles and surface tension. Density was calculated using an electronic scale in RADWAG products using SEM. The topographies of the perovskite films were analyzed by atomic force microscopy (AFM, Bruker) with Icon-PT-PLUS using tapping mode and Kelvin probe force microscope (KPFM, Bruker). Scanning electron microscopy(SEM) images of the device structure were measured using a Hitachi (S-2700, Japan). Electrical impedance spectroscopy (EIS) was performed using an Ivium compactStat.h electrochemical analyzer. Photoluminescence (PL) spectra were recorded using a Photon Technology International Fluorimeter (PTI, USA). The irradiated current density–voltage (J–V) curves were tested using Keithley 2400 under air mass 1.5 global (AM 1.5G) irradiation (100 mW cm^{-2}). The light intensity was calibrated using an NREL-Si solar cell. The external quantum efficiency (EQE) was measured under monochromatic light using a Xenon lamp (Dongwoo Optron).

3. Results and discussion

Infiltration of p-type HTMs as passivating materials into grain boundaries in inverted p-i-n PeSCs provides many advantages. It passivates the defect sites and removes the hydrophilic perovskite intermediate from the top to the bottom of the grain boundaries [37]. In particular, the selective charge transport properties of HTM allow only hole injection from the perovskite active layer near the grain boundaries and transport holes to the anode, leading to higher internal quantum efficiency (IQE) of the device. Fig. 1a presents the structure of the fully covered perovskite active layer with HTM for PeSC. The p-DTS $(FBTTh_2)_2$ was used in this work as a HTM. Since p-DTS$(FBTTh_2)_2$ has an upper conduction band (CB) edge and valence band (VB) edge higher than that of the perovskites active layer, the holes generated in the perovskite active layer easily move to the p-DTS$(FBTTh_2)_2$ without encountering any barrier, whereas the electrons are blocked because of the energy barrier at the interfaces. In addition, the hydrophobicity of p-DTS$(FBTTh_2)_2$ suppresses the decomposition of the perovskite by moisture, which increases the moisture stability of the PeSC.

Successful infiltration of the HTM into the grain boundaries has hardly been demonstrated so far due to the absence of an effective method with sufficient infiltration force. When the HTM was deposited by the conventional spin coating method, most materials were distributed on the surface of the perovskite layer and no infiltration of HTM into such narrow grain boundaries occurs owing to insufficient infiltrating force [38]. Randomly distributed HTM materials on the top surface of perovskite act as defect sites [39]. In an effort to overcome this issue, we have developed a new MS film formation process for infiltrating the HTM into grain boundaries. Fig. 1b presents the film fabrication process of the MS method. The process for fabricating perovskite films is exactly the same as the merged annealing process until the deposition of the HTM layer [40]. Our earlier work demonstrated that the merged annealing method produced enlarged grains with high crystallinity [40]. In contrast to the conventional spin-coating (SC) process with continuous spinning until complete film formation, our MS method included a momentary spinning process with a very short spinning time and subsequent drying process for complete film formation. After dripping the HTM solution on the perovskite layer rinsed with CB solvent, the substrate was spun for a spinning time of only 1 s. The complete HTM layer was finally obtained after drying. After that, the complete HTM layer on the perovskite film is re-spun, and then the HTM on the perovskite surface is washed out by dripping the CB solvent on the spinning substrate. Due to centrifugal force during substrate spinning, the CB enables the HTM to be washed only on the surface of the perovskite and HTM infiltrated into the grain boundaries is still present. The detailed procedure pictures of the MS method are compared with those of the conventional methods in Fig. S1.

Because the complete film was hardly obtained with such a short spinning time of 1 s, the remaining solution of the HTM is still moveable even after momentary spinning. When the substrate is spun, the HTM solution spreads from the center to the edge due to centrifugal force, while the solution moves back to the center from the edge after stopping

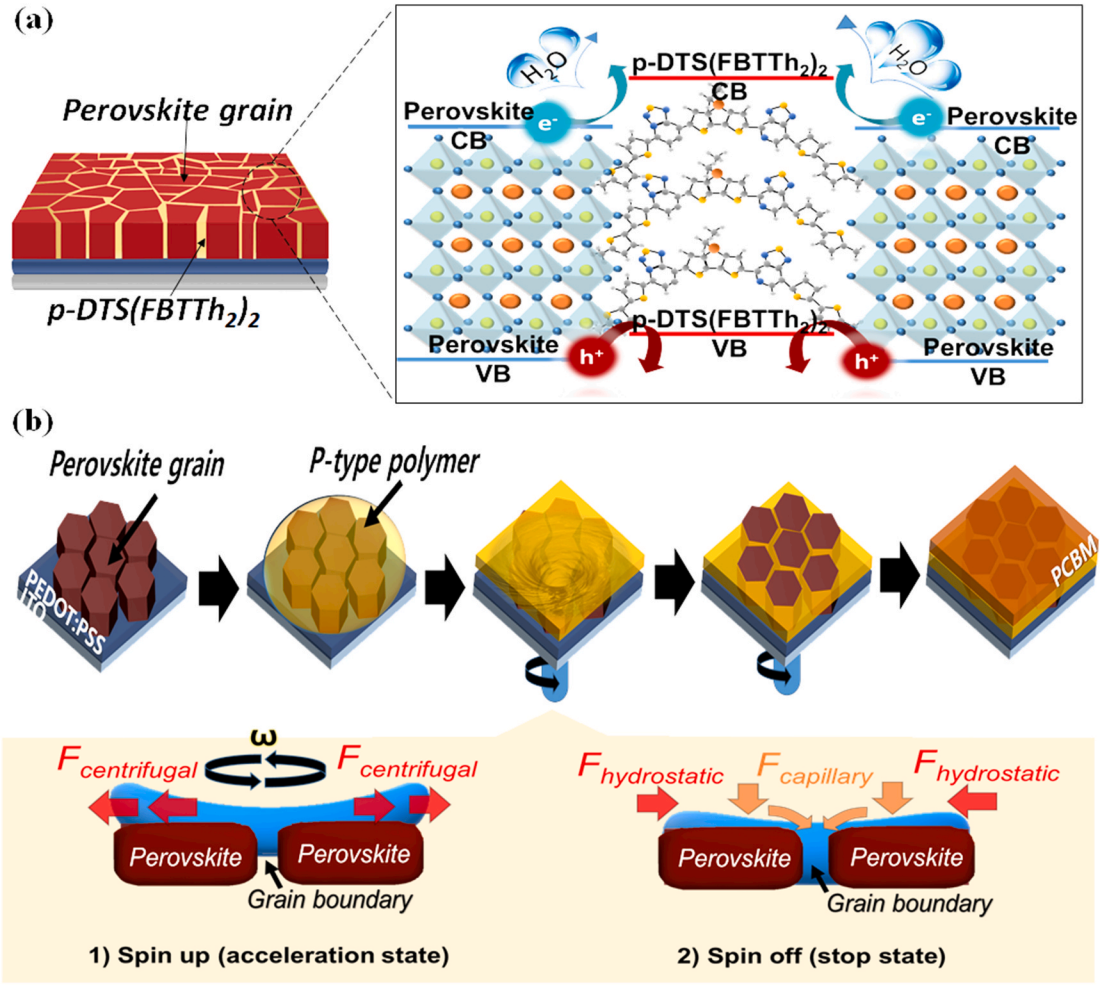

Fig. 1. (a) Conceptual diagram of charge transport in perovskite film with infiltration of hole transport material into grain boundaries. (b) Fabricating process for the momentary spinning method (inset: illustration of solution movement on and off the substrate spinning).

the spinning. The inset of Fig. 1b illustrates the solution movement on and off the substrate spinning. Previous works by Willson's research group have demonstrated that the solution after stopping substrate spinning immediately began to planarize under capillary and hydrostatic forces [41]. Therefore, it is expected that the capillary force induced by stopping the spinning in the MS process can act as the infiltration force for the HTM infiltration into the grain boundaries. Fig. S2 presents pictures of the films prepared by drop casting without spinning, conventional SC, and our MS methods. All films were first washed out by CB dripping under film spinning conditions. When we washed the films with CB solvent again without spinning, only the MS film exhibited dissolved materials with colored solution, whereas the other films showed the original colorless CB solvent. Because the infiltrated HTM was hardly washed out by dripping the CB on the spinning film, the dissolved materials originated from the infiltrated HTM into grain boundaries, indicating that the MS method produces infiltration of the HTM into grain boundaries.

It is known that the infiltration force is influenced by the concentration of HTM because of capillary pressure, as represented by the Young–Laplace equation ($P = f(\theta,r)p(r) = 2\gamma cos\,\theta p(r)$, where, r and θ are the surface tension of the liquid and the contact angle, respectively) [42]. Because the capillary pressure is sensitive to the surface tension of a penetrant and its contact angle [43], which are affected by the concentration of the solution, an optimizing concentration of the HTM solution is determined to achieve efficient infiltration of the HTM into grain boundaries. Fig. 2a presents the variations in the contact angle and surface tension of the HTM solution with increasing concentration of HTM. Dissolution of HTM in a CB solvent with a concentration of 0.1% w/v. slightly increases the surface tension and contact angle, and the surface tension does not noticeably change up to 0.5–1.3% w/v, while its contact angle continuously increased until 1.3% w/v. Corresponding infiltration forces were calculated using the Young-Laplace equation and are presented in Fig. 2b. The infiltration force is not very sensitive to an increase in concentration until 0.5% w/v with almost constant intensity. However, the force quickly decreases with increasing concentration above 0.5% w/v. Therefore, we fixed the concentration of HTM at 0.5% w/v. The infiltration force is also influenced by the rotational speed related to the centrifugal force. After measuring the density of the perovskite layer, we selected 2000 rpm as the optimized speed. Table S1 summarizes the density of the filled-perovskite layer for different spinning speeds.

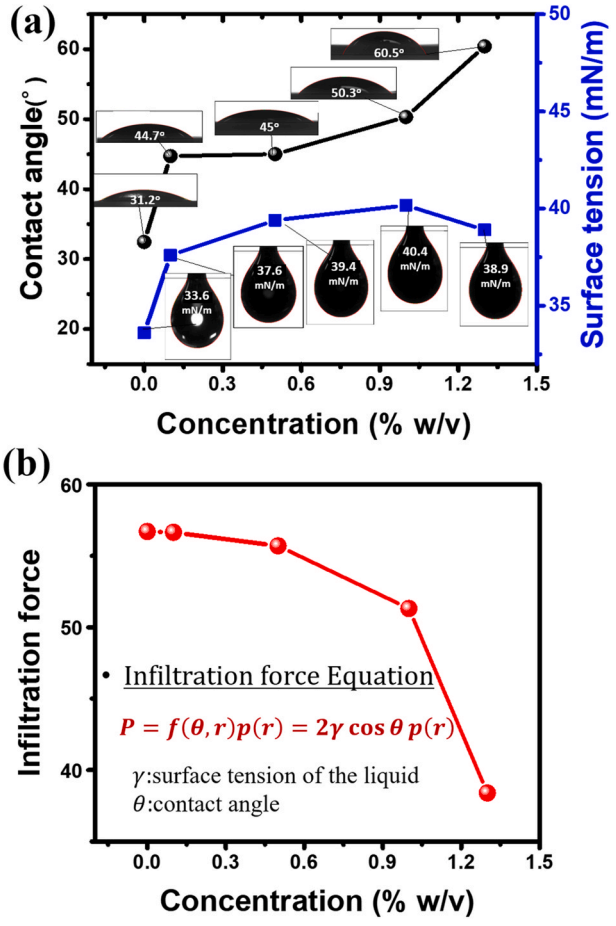

Fig. 2. (a) Contact angles and surface tension variations for different HTM concentrations (b) the change of infiltration force with increasing HTM concentrations.

To verify the infiltration of the HTM into the grain boundaries, we checked the morphologies of the films prepared by the SC and MS methods. Fig. 3a and b presents the atomic force microscopy (AFM) and Kelvin probe force microscope (KPFM) images of the films fabricated by the SC and MS method (namely SC film and MS film here), respectively. Owing to the similarity of the film fabrication process between them, except for the existence of an infiltration force, both the SC and MS films present similar morphologies with enlarged grains and apparent grain boundaries. However, the root-mean-square (RMS) surface roughness and the surface potential between the grain and the grain boundary of the films were slightly different. Enhanced smoothness between the grains was observed in the MS film with relatively low RMS values of 3.77 nm compared to 12.20 nm for the SC film. In addition, the KPFM images provide quite a different potential distribution between both films. While the SC film exhibits a uniform distribution of the surface potentials on the entire surface, the MS film shows a distinct potential difference between grains when we measure the surface potential around grain boundaries. Because the difference in surface potential usually originates from different components, we attribute the potential difference in the MS film to the existence of HTM between $MAPbI_3$ perovskite grains.

In order to verify our expectation, we have performed SEM-EDS measurements for the films. Since the HTM includes Silicon, which isn't present in $MAPbI_3$ perovskite, we have specifically checked the Pb and Si elements in the films. Fig. 3c and d shows the top view of the SEM image of the SC and MS films. As expected, while the yellow-colored Pb element was observed in both films, a greenish-blue Si element was only detected in the MS film. In particular, the shape of the distribution of the Si elements in the film resembles the morphology of the film obtained by SEM. This tendency is also observed in the cross-sectional images of SEM-EDS for the films, as shown in Fig. 3e and f. The Si elements were only present in the MS film and were located at the grain boundaries. In addition, the XPS depth data in Fig. 3g and h confirm the existence of HTM in the MS film. Based on these data, we conclude that the HTM is infiltrated into the grain boundaries by our MS method.

Since the MS films provide infiltration of HTM into grain boundaries, leading to enhanced hole transport, it is expected that the device with the MS film has improved electrical properties compared to conventional devices. Therefore, we first measured the dark current-voltage curves of the devices fabricated by the MS and SC methods to investigate the carrier recombination properties. Fig. 4a shows the device structure used in this work. Both devices have almost the same device structure as glass/ITO/PEDOT:PSS/$MAPbI_3$/PCBM/Al. Compared to the SC device, the MS device has an additional infiltration component of the HTM into the grain boundaries. Fig. 4b exhibits current density values against applying voltages from −1.5 V to +1.5 V under dark condition, respectively. Both devices exhibit conventional semiconducting properties with clear rectification under an applied bias. When a forward bias higher than 0.8 V is applied to both devices, the charge carriers begin to inject to the perovskite active layer and the current increases gradually with an increase in the applied bias. However, the current flow is suppressed under negative bias conditions owing to the large energy barrier for charge injection. Although similar current behavior in both devices is

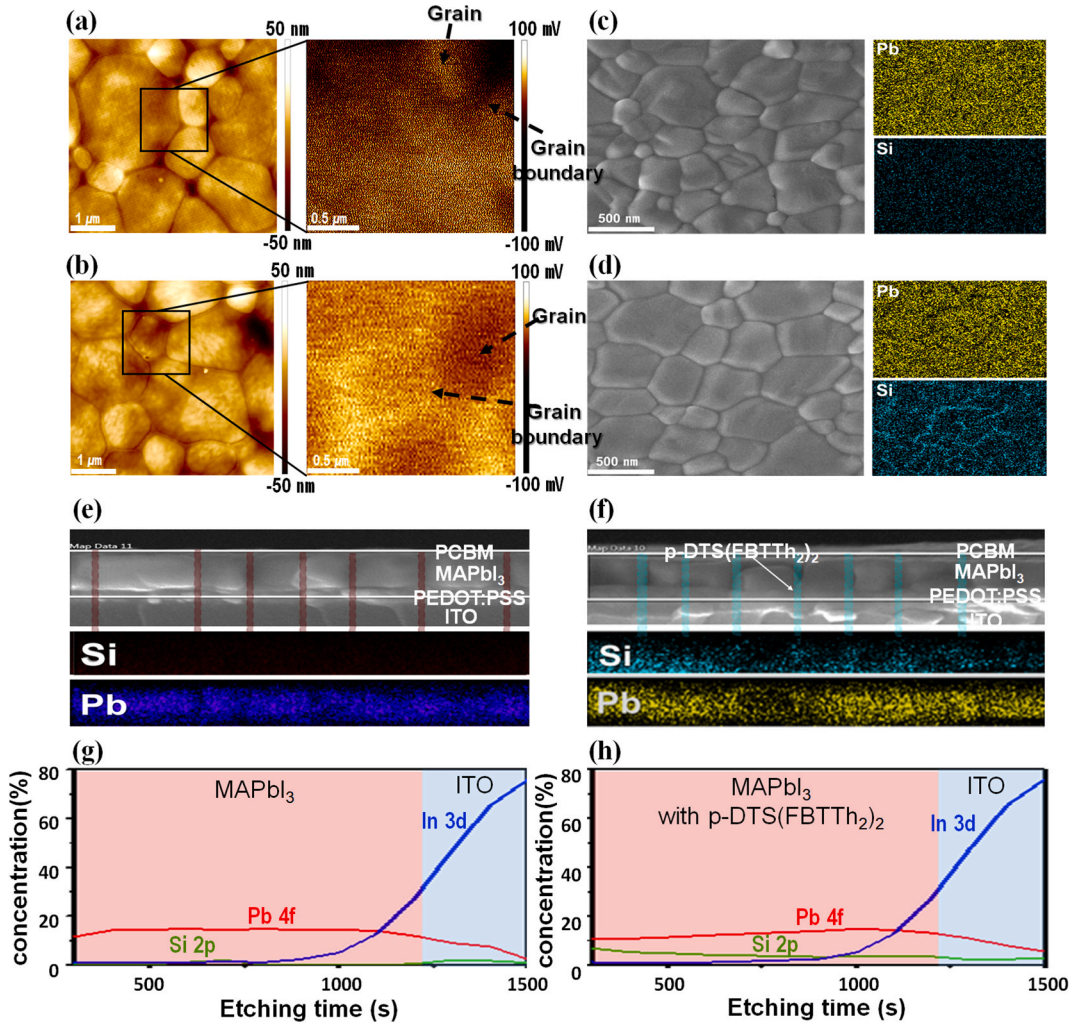

Fig. 3. AFM, KPFM, SEM-EDS images and XPS depth data of the perovskite films prepared by conventional SC (a,c,e,g) and MS (b,d,f,h) methods.

observed due to identical device components with identical energy levels, there are noticeable differences in current values. At zero voltage, the MS device shows a lower current of 0.0019 mA/cm^2 and a reduced leakage current under all negative bias conditions compared to the SC device with a current of 0.0030 mA/cm^2. In addition, the MS device presents better current flow under strong forward bias conditions (see the inset of Fig. 4b). These results clearly imply that infiltration of the HTM in the MS device can suppress non-radiative recombination and reduce shunting paths in the device.

Further investigation of the effect of HTM on the charge transport properties and electrical impedance spectroscopy (EIS) measurements was performed to observe the internal electrical processes of the PeSC. Fig. 4c presents Nyquist plots of MS (red line) and SC (black line) devices at 4 MHz–0.1 Hz at −0.7 V under dark conditions. The corresponding equivalent circuit obtained by conventional fitting is presented in the inset. The circuit is composed of a series of resistance R_s and a parallel resistance R_p with a corresponding capacitance element. As shown in Fig. 4c, it is evident that the MS devices with infiltration of the HTM exhibit a much larger diameter of the semicircle (red line) compared to the SC device (black line), which corresponds to the higher R_p resistance of the device. Because R_p corresponds to recombination resistance($\mathbf{R_{rec}}$) in PeSC, a higher R_p of the MS devices results in suppressed interfacial charge recombination and improved charge extraction. This result matches well with the dark J–V curve characteristics in Fig. 4b.

To further verify the improvement of charge transport by reducing the electrical trap, we analyzed the hole trap density and hole mobility by using the space-charge limited current (SCLC) model in Fig. 4d. The device structure for hole mobility measurement is ITO/PEDOT:PSS/perovskite/MoO_3/Ag. The results were calculated for trap state density by using trap-filled limit voltage equation ($V_{TFL} = en_tL^2/2\varepsilon\varepsilon_0$, where, e, n_t, L, ε, and ε_0 are the electric charge, trap-state density, the thickness of perovskite film, relative dielectric constant of perovskite, and vacuum permittivity respectively). As summarized in Table 1, the MS device has a lower trap states density of 1.38×10^{15} cm^{-3} and a higher hole mobility of 1.96×10^{-3} cm^2/V·s compared to the SC device with a trap states density of 2.29×10^{15} cm^{-3} and hole mobility of 5.12×10^{-4} cm^2/V·s. Electron trap density and mobility also have same tendency (Fig. S3). In addition, the decrease in PL intensity in the MS film, as shown in Fig. S3, demonstrates enhanced hole transport near the grain boundaries to the HTM materials into the grain boundaries. Based on these results, we conclude that the infiltration of the HTM leads to better charge extraction with improved hole mobility.

Fig. 5a depicts the J–V characteristics of the MS and SC PeSCs measured under AM 1.5 G (100 mW cm^{-2}) irradiation conditions.

As expected, the MS PeSC demonstrates an enhanced device performance with higher J_{sc}, higher V_{oc}, and higher FF compared to the SC device. The distribution of the PCE and the detailed photovoltaic parameters of the PeSCs with various HTM concentration are provided in Fig. 5b, Fig. S4 and Table 2. All photovoltaic parameters of Jsc, Voc and FF increase with increasing concentration of the HTM up to 0.5% w/v due to passivation effect. However, they decrease with increasing concentration higher than 0.5% w/v because the remaining HTM on the top

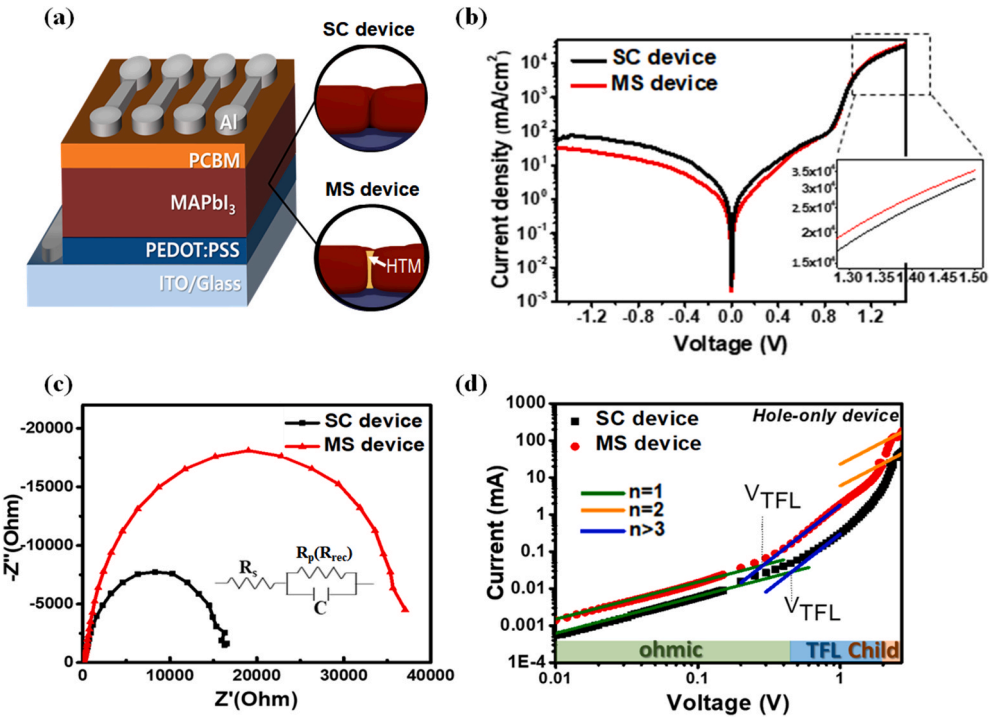

Fig. 4. (a) Device structure, (b) dark J-V curve and (c) electrical impedance spectra (EIS). (d) The characteristics of hole mobility and trap state density of SC and MS hole-only devices.

Table 1
The hole mobility and trap state density of the SC device and MS device.

Device	Trap states density [cm^{-3}]	Hole Mobility [$cm^2V^{-1}S^{-1}$]
MS	1.38×10^{15}	1.96×10^{-3}
SC	2.29×10^{15}	5.12×10^{-4}

of perovskite surface hinders the charge transport. The best MS device has a J_{sc} of 23.2 mA cm^{-2}, a V_{oc} of 0.99 V, and an FF of 0.81, yielding an efficiency of 18.6%. Because both devices have almost the same device structure and perovskite active layer thickness, which affects the amount of photon absorption, the enhanced device performance in the MS PeSC is attributed to the improved IQE compared to SC PeSC. In addition, considering the similar morphology of the perovskite active layer of the MS device, except the infiltration of the HTM into grain boundaries (see the AFM and SEM images of Fig. 3a–d), we believe that the improved IQE in the MS device mainly originates from the decreased defect sites around the grain boundaries by passivation of the HTM. In addition, improved hole carrier transport is ascribed to enhanced hole mobility and an additional hole transport channel generated in the HTM. Fig. 5c presents incident photon to current efficiency (IPCE) of the corresponding MS PeSCs and SC PeSCs. The MS device exhibits an enhanced IPCE at the entire wavelength range of 400–800 nm compared to the SC device. This enhancement in the IPCE for the MS device is well matched to the higher J_{sc} in the J–V curve in Fig. 5a and Fig. S5. Furthermore, we confirmed the enhancement in device performance of PeSCs by using various HTMs with P3HT, PTAA, and PTB7-Th as HTM materials. As depicted in Fig. S6 and Table S2, the devices with infiltration of the HTMs present increased device performance compared to the pristine device. These results confirmed the effect of infiltration of HTM with selective charge transport on the enhancement of device performance.

For detailed comprehension of the enhanced device performance in MS PeSC, some straightforward insights into the charge recombination process within devices were achieved by analyzing the light intensity dependence of J_{sc} and V_{oc}. The dependence of J_{sc} on the logarithmic form of the incident light intensity (I) based on $J_{sc} \propto I^{\alpha}$ is shown in Fig. 5d. While the J_{sc} of both devices exhibit a linear relationship with respect to the light intensity, the slope of the MS devices with a gradient value of $\alpha = 0.91$ is greater than the value of $\alpha = 0.84$ of the SC device, implying decreased bimolecular recombination under short-circuit conditions. Fig. 5e illustrates the light dependence of V_{oc} on I in logarithmic form (ln(I)), which fits the equation ($V_{oc} = \varepsilon\, kTln(I)/q + (a$ constant), where, ε, k, T, and q are the ideal factor, Boltzmann constant, absolute temperature, and elementary charge, respectively). The ε value of the MS device was calculated to be 1.07, which is closer to 1 than that of the SC device with a value of 1.19. The reduced ε value in the MS device also proves the effective inhibition of trap-assisted charge recombination and the high carrier mobility induced by infiltration of the HTM into grain boundaries. Therefore, it is worth noting that infiltration of HTM into grain boundaries using the MS method leads to reduced charge recombination and improved charge collection and a consequent enhancement in device performance.

In parallel, since the hydrophilic grain boundaries are passivated with hydrophobic HTM in the MS PeSC, it is expected that the MS PeSC present improved moisture stability compared to SC PeSC. Fig. 5f demonstrates the device stability in the dry box without encapsulation. After 20 days of storage, the PCE of the SC device decreased by approximately 50%, whereas only 20% of the initial PCE was lost for the MS device. In addition, the MS device exhibits improved stability with a slower decrease in J_{sc} compared with the SC device under ambient environment for 7 days (Fig. S7). This improvement of stability in the MS PeSCs is easily understood by the enhancement in the hydrophobicity of the perovskite film via passivation of hydrophilic grain boundaries, which was confirmed by contact angle measurement, as shown in Fig. S8.

4. Conclusion

In conclusion, we developed an effective MS method for infiltrating HTM into grain boundaries. By using a momentary spinning process with a very short spinning time, we successfully demonstrated

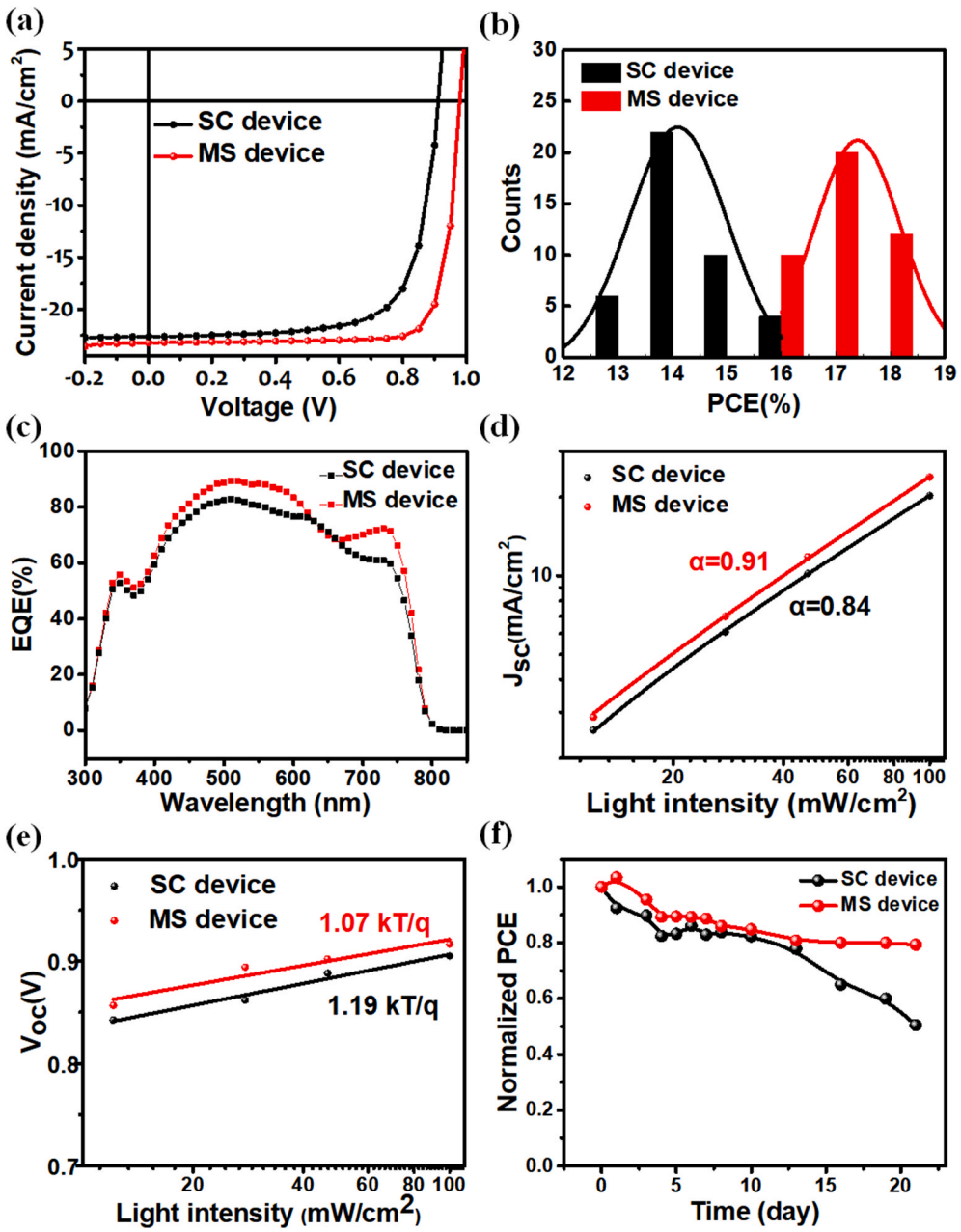

Fig. 5. (a) J-V curves, (b) device performance distribution, (c) the IPCE spectra, (d) J_{sc} vs. light intensity and (e) V_{oc} vs. light intensity, and (f) the device stability test of the corresponding perovskite solar cells under nitrogen glove box environment (H_2O 55 ppm, O_2 5 ppm) at room temperature.

Table 2
The parameters of the SC and MS device.

Device	J_{sc} [mAcm^{-2}]	V_{oc} [V]	FF	$PCE_{opt.}$ [%]
SC	22.5 ± 0.74	0.95 ± 0.02	0.77 ± 0.02	16.5 ± 0.88
MS	23.2 ± 0.79	0.99 ± 0.03	0.81 ± 0.03	18.6 ± 0.46

infiltration of HTM into grain boundaries. The perovskite active layer prepared by the MS method provides highly crystalline enlarged gains and fully passivated grain boundaries. Furthermore, the MS PeSC device exhibits remarkable enhancement in device performance with higher J_{sc}, higher V_{oc}, and higher FF compared to the SC device. The best MS device has a J_{sc} of 23.2 mA cm^{-2}, a V_{oc} of 0.99 V, and an FF of 0.81, yielding an efficiency of 18.6%. The improved device performance is ascribed to reduced charge recombination and improved charge collection via infiltrated HTM with selective charge transport into grain boundaries. In addition, the hydrophobicity of the HTM leads to improved moisture stability of the device. After 20 days of storage, the MS device exhibited improved stability with over 80% of the initial PCE compared to the SC device with only 50%. We believe that our MS method can improve the performance and stability of perovskite solar cells.

CRediT authorship contribution statement

Danbi Kim: Conceptualization, Methodology, Writing – original draft. **Insoo Shin:** Formal analysis, Writing – review & editing, Supervision. **Hyun-Seock Yang:** Investigation, Formal analysis, Visualization. **Pesi Mwitumwa Hangoma:** Formal analysis, Visualization. **Jong Seong Bae:** Formal analysis, Validation. **Bo Ram Lee:** Resources, Validation. **Joo Hyun Kim:** Resources, Validation. **Doo Kyung Moon:** Resources, Validation. **Sung Heum Park:** Supervision, Project

administration.

Declaration of competing interest

The authors declare that they have no known competing financial interests or personal relationships that could have appeared to influence the work reported in this paper.

Acknowledgements

This research work was supported by the New & Renewable Energy Core Technology Program of the Korea Institute of Energy Technology Evaluation and Planning (KETEP) granted financial resource from the Ministry of Trade, Industry & Energy, Republic of Korea (20193091010110). This research was also supported by the NRF Grant funded by the Korean Government (2020R1A2B5B01001611, 2021M3H4A1A02057007).

Appendix A. Supplementary data

Supplementary data to this article can be found online at https://doi.org/10.1016/j.jpowsour.2021.230212.

References

[1] S.D. Stranks, G.E. Eperon, G. Grancini, C. Menelaou, M.J.P. Alcocer, T. Leijtens, L. M. Herz, A. Petrozza, H.J. Snaith, Electron-hole diffusion lengths exceeding 1 micrometer in an organometal trihalide perovskite absorber, Science 342 (2013) 341–344, https://doi.org/10.1126/science.1243982.

[2] A. Miyata, A. Mitioglu, P. Plochocka, O. Portugall, J.T.-W. Wang, S.D. Stranks, H. J. Snaith, R.J. Nicholas, Direct measurement of the exciton binding energy and effective masses for charge carriers in organic–inorganic tri-halide perovskites, Nat. Phys. 11 (2015) 582–587, https://doi.org/10.1038/nphys3357.

[3] D. Shi, V. Adinolfi, R. Comin, M. Yuan, E. Alarousu, A. Buin, Y. Chen, S. Hoogland, A. Rothenberger, K. Katsiev, Y. Losovyj, X. Zhang, P.A. Dowben, O.F. Mohammed, E.H. Sargent, O.M. Bakr, Low trap-state density and long carrier diffusion in organolead trihalide perovskite single crystals, Science 347 (2015) 519–522, https://doi.org/10.1126/science.aaa2725.

[4] R.J. Sutton, G.E. Eperon, L. Miranda, E.S. Parrott, B.A. Kamino, J.B. Patel, M. T. Hörantner, M.B. Johnston, A.A. Haghighirad, D.T. Moore, H.J. Snaith, Bandgap-tunable cesium lead halide perovskites with high thermal stability for efficient solar cells, Adv. Energy Mater. 6 (2016) 1502458, https://doi.org/10.1002/aenm.201502458.

[5] National center for photovoltaics (NCPV) at the National Renewable energy laboratory (NREL). https://www.nrel.gov/pv/assets/pdfs/best-research-celleffici encies.20200203.pdf (accessed 12 October 2020).

[6] C. Bi, Q. Wang, Y. Shao, Y. Yuan, Z. Xiao, J. Huang, Non-wetting surface-driven high-aspect-ratio crystalline grain growth for efficient hybrid perovskite solar cells, Nat. Commun. 6 (2015) 7747, https://doi.org/10.1038/ncomms8747.

[7] W. Nie, H. Tsai, R. Asadpour, J.-C. Blancon, A.J. Neukirch, G. Gupta, J.J. Crochet, M. Chhowalla, S. Tretiak, M.A. Alam, H.-L. Wang, A.D. Mohite, High-efficiency solution-processed perovskite solar cells with millimeter-scale grains, Science 347 (2015) 522–525, https://doi.org/10.1126/science.aaa0472.

[8] L. Li, Y. Chen, Z. Liu, Q. Chen, X. Wang, H. Zhou, The additive coordination effect on hybrids perovskite crystallization and high-performance solar cell, Adv. Mater. 28 (2016) 9862–9868, https://doi.org/10.1002/adma.201603021.

[9] T. Singh, T. Miyasaka, Stabilizing the efficiency beyond 20% with a mixed cation perovskite solar cell fabricated in ambient air under controlled humidity, Adv. Energy Mater. 8 (2018) 1700677, https://doi.org/10.1002/aenm.201700677.

[10] H. Uratani, K. Yamashita, Charge carrier trapping at surface defects of perovskite solar cell absorbers: a first-principles study, J. Phys. Chem. Lett. 8 (2017) 742–746, https://doi.org/10.1021/acs.jpclett.7b00055.

[11] C. Ran, J. Xu, W. Gao, C. Huang, S. Dou, Defects in metal triiodide perovskite materials towards high-performance solar cells: origin, impact, characterization, and engineering, Chem. Soc. Rev. 47 (2018) 4581–4610, https://doi.org/10.1039/C7CS00868F.

[12] D.-Y. Son, J.-W. Lee, Y.J. Choi, I.-H. Jang, S. Lee, P.J. Yoo, H. Shin, N. Ahn, M. Choi, D. Kim, N.-G. Park, Self-formed grain boundary healing layer for highly efficient CH3NH3PbI3 perovskite solar cells, Nat. Energy 1 (2016) 16081, https://doi.org/10.1038/nenergy.2016.81.

[13] S. Ye, H. Rao, Z. Zhao, L. Zhang, H. Bao, W. Sun, Y. Li, F. Gu, J. Wang, Z. Liu, Z. Bian, C. Huang, A breakthrough efficiency of 19.9% obtained in inverted perovskite solar cells by using an efficient trap state passivator Cu(thiourea)I, J. Am. Chem. Soc. 139 (2017) 7504–7512, https://doi.org/10.1021/jacs.7b01439.

[14] T.S. Sherkar, C. Momblona, L. Gil-Escrig, J. Ávila, M. Sessolo, H.J. Bolink, L.J. A. Koster, Recombination in perovskite solar cells: significance of grain boundaries, interface traps, and defect ions, ACS Energy Lett 2 (2017) 1214–1222, https://doi.org/10.1021/acsenergylett.7b00236.

[15] S. Shao, J. Liu, G. Portale, H.-H. Fang, G.R. Blake, G.H. ten Brink, L.J.A. Koster, M. A. Loi, Highly reproducible Sn-based hybrid perovskite solar cells with 9% efficiency, Adv. Energy Mater. 8 (2018) 1702019, https://doi.org/10.1002/aenm.201702019.

[16] B. Chen, P.N. Rudd, S. Yang, Y. Yuan, J. Huang, Imperfections and their passivation in halide perovskite solar cells, Chem. Soc. Rev. 48 (2019) 3842–3867, https://doi.org/10.1039/C8CS00853A.

[17] B. Conings, J. Drijkoningen, N. Gauquelin, A. Babayigit, J. D'Haen, L. D'Olieslaeger, A. Ethirajan, J. Verbeeck, J. Manca, E. Mosconi, F. De Angelis, H.-G. Boyen, Intrinsic thermal instability of methylammonium lead trihalide perovskite, Adv. Energy Mater. 5 (2015) 1500477, https://doi.org/10.1002/aenm.201500477.

[18] Q. Wang, B. Chen, Y. Liu, Y. Deng, Y. Bai, Q. Dong, J. Huang, Scaling behavior of moisture-induced grain degradation in polycrystalline hybrid perovskite thin films, Energy Environ. Sci. 10 (2017) 516–522, https://doi.org/10.1039/C6EE02941H.

[19] Z. Xiao, Q. Dong, C. Bi, Y. Shao, Y. Yuan, J. Huang, Solvent annealing of perovskite-induced crystal growth for photovoltaic-device efficiency enhancement, Adv. Mater. 26 (2014) 6503–6509, https://doi.org/10.1002/adma.201401685.

[20] P. You, G. Li, G. Tang, J. Cao, F. Yan, Ultrafast laser-annealing of perovskite films for efficient perovskite solar cells, Energy Environ. Sci. 13 (2020) 1187–1196, https://doi.org/10.1039/C9EE02324K.

[21] Y. Yang, J. Wu, X. Wang, Q. Guo, X. Liu, W. Sun, Y. Wei, Y. Huang, Z. Lan, M. Huang, J. Lin, H. Chen, Z. Wei, Suppressing vacancy defects and grain boundaries via ostwald ripening for high-performance and stable perovskite solar cells, Adv. Mater. 32 (2020) 1904347, https://doi.org/10.1002/adma.201904347.

[22] G. Grancini, C. Roldán-Carmona, I. Zimmermann, E. Mosconi, X. Lee, D. Martineau, S. Narbey, F. Oswald, F. De Angelis, M. Graetzel, M.K. Nazeeruddin, One-Year stable perovskite solar cells by 2D/3D interface engineering, Nat. Commun. 8 (2017) 15684, https://doi.org/10.1038/ncomms15684.

[23] Z. Wang, Q. Lin, F.P. Chmiel, N. Sakai, L.M. Herz, H.J. Snaith, Efficient ambient-air-stable solar cells with 2D–3D heterostructured butylammonium-caesium-formamidinium lead halide perovskites, Nat. Energy 2 (2017) 17135, https://doi.org/10.1038/nenergy.2017.135.

[24] Y. Hu, T. Qiu, F. Bai, W. Ruan, S. Zhang, Highly efficient and stable solar cells with 2D MA 3 Bi 2 I 9/3D MAPbI 3 heterostructured perovskites, Adv. Energy Mater. 8 (2018) 1703620, https://doi.org/10.1002/aenm.201703620.

[25] G. Liu, H. Zheng, X. Xu, S. Xu, X. Zhang, X. Pan, S. Dai, Introduction of hydrophobic ammonium salts with Halogen functional groups for high-efficiency and stable 2D/3D perovskite solar cells, Adv. Funct. Mater. 29 (2019) 1807565, https://doi.org/10.1002/adfm.201807565.

[26] P. Guo, Q. Ye, X. Yang, J. Zhang, F. Xu, D. Shchukin, B. Wei, H. Wang, Surface & grain boundary co-passivation by fluorocarbon based bifunctional molecules for perovskite solar cells with efficiency over 21%, J. Mater. Chem. A. 7 (2019) 2497–2506, https://doi.org/10.1039/C8TA11524A.

[27] H. Kim, S. Lee, D.Y. Lee, M.J. Paik, H. Na, J. Lee, S. Il Seok, Optimal interfacial engineering with different length of alkylammonium halide for efficient and stable perovskite solar cells, Adv. Energy Mater. 9 (2019) 1902740, https://doi.org/10.1002/aenm.201902740.

[28] E.A. Alharbi, A.Y. Alyamani, D.J. Kubicki, A.R. Uhl, B.J. Walder, A.Q. Alanazi, J. Luo, A. Burgos-Caminal, A. Albadri, H. Albrithen, M.H. Alotaibi, J.-E. Moser, S. M. Zakeeruddin, F. Giordano, L. Emsley, M. Grätzel, Atomic-level passivation mechanism of ammonium salts enabling highly efficient perovskite solar cells, Nat. Commun. 10 (2019) 3008, https://doi.org/10.1038/s41467-019-10985-5.

[29] T. Niu, J. Lu, R. Munir, J. Li, D. Barrit, X. Zhang, H. Hu, Z. Yang, A. Amassian, K. Zhao, S.F. Liu, Stable high-performance perovskite solar cells via grain boundary passivation, Adv. Mater. 30 (2018) 1706576, https://doi.org/10.1002/adma.201706576.

[30] W. Chen, Y. Zhou, L. Wang, Y. Wu, B. Tu, B. Yu, F. Liu, H.-W. Tam, G. Wang, A. B. Djurišić, L. Huang, Z. He, Molecule-doped nickel oxide: verified charge transfer and planar inverted mixed cation perovskite solar cell, Adv. Mater. 30 (2018) 1800515, https://doi.org/10.1002/adma.201800515.

[31] Y. Bai, Y. Lin, L. Ren, X. Shi, E. Strounina, Y. Deng, Q. Wang, Y. Fang, X. Zheng, Y. Lin, Z.-G. Chen, Y. Du, L. Wang, J. Huang, Oligomeric silica-wrapped perovskites enable synchronous defect passivation and grain stabilization for efficient and stable perovskite photovoltaics, ACS Energy Lett 4 (2019) 1231–1240, https://doi.org/10.1021/acsenergylett.9b00608.

[32] X. Zheng, Y. Hou, C. Bao, J. Yin, F. Yuan, Z. Huang, K. Song, J. Liu, J. Troughton, N. Gasparini, C. Zhou, Y. Lin, D.-J. Xue, B. Chen, A.K. Johnston, N. Wei, M. N. Hedhili, M. Wei, A.Y. Alsalloum, P. Maity, B. Turedi, C. Yang, D. Baran, T. D. Anthopoulos, Y. Han, Z.-H. Lu, O.F. Mohammed, F. Gao, E.H. Sargent, O. M. Bakr, Managing grains and interfaces via ligand anchoring enables 22.3%-efficiency inverted perovskite solar cells, Nat. Energy 5 (2020) 131–140, https://doi.org/10.1038/s41560-019-0538-4.

[33] E.D. Jung, A.K. Harit, D.H. Kim, C.H. Jang, J.H. Park, S. Cho, M.H. Song, H.Y. Woo, Multiply charged conjugated polyelectrolytes as a multifunctional interlayer for efficient and scalable perovskite solar cells, Adv. Mater. 32 (2020) 2002333, https://doi.org/10.1002/adma.202002333.

[34] Y. Shao, Z. Xiao, C. Bi, Y. Yuan, J. Huang, Origin and elimination of photocurrent hysteresis by fullerene passivation in CH3NH3PbI3 planar heterojunction solar cells, Nat. Commun. 5 (2014) 5784, https://doi.org/10.1038/ncomms6784.

[35] F. Cai, J. Cai, L. Yang, W. Li, R.S. Gurney, H. Yi, A. Iraqi, D. Liu, T. Wang, Molecular engineering of conjugated polymers for efficient hole transport and defect passivation in perovskite solar cells, Nano Energy 45 (2018) 28–36, https://doi.org/10.1016/j.nanoen.2017.12.028.

[36] P. Zhu, S. Gu, X. Luo, Y. Gao, S. Li, J. Zhu, H. Tan, Simultaneous contact and grain-boundary passivation in planar perovskite solar cells using SnO 2 -KCl composite

electron transport layer, Adv. Energy Mater. 10 (2020) 1903083, https://doi.org/10.1002/aenm.201903083.
[37] H. Back, G. Kim, H. Kim, C.-Y. Nam, J. Kim, Y.R. Kim, T. Kim, B. Park, J.R. Durrant, K. Lee, Highly stable inverted methylammonium lead tri-iodide perovskite solar cells achieved by surface re-crystallization, Energy Environ. Sci. 13 (2020) 840–847, https://doi.org/10.1039/C9EE03736E.
[38] P. Zhao, B.J. Kim, H.S. Jung, Passivation in perovskite solar cells: a review, Mater. Today Energy 7 (2018) 267–286, https://doi.org/10.1016/j.mtener.2018.01.004.
[39] H. Wang, Z. Wang, Z. Yang, Y. Xu, Y. Ding, L. Tan, C. Yi, Z. Zhang, K. Meng, G. Chen, Y. Zhao, Y. Luo, X. Zhang, A. Hagfeldt, J. Luo, Ligand-modulated excess PbI 2 nanosheets for highly efficient and stable perovskite solar cells, Adv. Mater. 32 (2020) 2000865, https://doi.org/10.1002/adma.202000865.
[40] Y. Liu, I. Shin, I.-W. Hwang, S. Kim, J. Lee, M.-S. Yang, Y.K. Jung, J.-W. Jang, J. H. Jeong, S.H. Park, K.H. Kim, Single-Crystal-like perovskite for high-performance solar cells using the effective merged annealing method, ACS Appl. Mater. Interfaces 9 (2017) 12382–12390, https://doi.org/10.1021/acsami.6b16541.
[41] C.G.W. Michael W. Lin, Brook H. Chao, Jianjun Hao, Kyle Osberg, Paul S. Ho, Simulation and design of planarizing materials for reverse-tone step and flash imprint lithography, J. Micro/Nanolithography, MEMS, MOEMS. 7 (2008), https://doi.org/10.1117/1.2896047, 023008.
[42] S. Smirnov, I. Vlassiouk, P. Takmakov, F. Rios, Water confinement in hydrophobic nanopores. Pressure-induced wetting and drying, ACS Nano 4 (2010) 5069–5075, https://doi.org/10.1021/nn101080k.
[43] N.A. Tracy, P.O. Moore, Nondestructive Testing Handbook, third ed., American Society for Nondestructive Testing Inc., USA, 2003.